

Direct Visualization of Localized Vibrations at Complex Grain Boundaries

Eric R. Hoglund,* De-Liang Bao, Andrew O'Hara, Thomas W. Pfeifer, Md Shafkat Bin Hoque, Sara Makarem, James M. Howe, Sokrates T. Pantelides,* Patrick E. Hopkins,* and Jordan A. Hachtel*

Grain boundaries (GBs) are a prolific microstructural feature that dominates the functionality of a wide class of materials. The functionality at a GB results from the unique atomic arrangements, different from those in the grain, that have driven extensive experimental and theoretical studies correlating atomic-scale GB structures to macroscopic electronic, infrared optical, and thermal properties. In this work, a SrTiO₃ GB is examined using atomic-resolution aberration-corrected scanning transmission electron microscopy and ultrahigh-energy-resolution monochromated electron energy-loss spectroscopy, in conjunction with density functional theory. This combination enables the correlation of the GB structure, nonstoichiometry, and chemical bonding with a redistribution of vibrational states within the GB dislocation cores. The new experimental access to localized GB vibrations provides a direct route to quantifying the impact of individual boundaries on macroscopic properties.

1. Introduction

The local atomic arrangement in a grain boundary (GB) is different from that in the bounding grains to enable the accommodation of the misorientation of the corresponding lattices.^[1–8] Structurally, the local arrangements comprise dislocation cores and structural units that repeat along the boundary. Chemically, dislocation cores and other structural units are not always stoichiometric and may even feature complexions.^[9] Together, the chemical and structural dissimilarities of GBs and grains lead to localized GB vibrations, which are of interest to many fields. For instance, in thermal transport^[4–7,10] and infrared optics,^[4,8] phonon frequencies and lifetimes dictate the key aspects of the material response. Additionally,

variations in the localized vibrations can significantly alter the free-energy landscape for functional materials^[11–13] or increase entropic contributions to free energy and influence phase transitions.^[14–16]


For simple systems, theoretical predictions have been used to describe the unique relation between the structure and chemistry at a single GB to its local vibrational properties.^[17–19] However, density functional theory (DFT) calculations of GBs with small misorientation angle, especially in materials with complex structure and stoichiometry, become increasingly challenging, as they may necessitate excessively large supercells. On the other hand, for the analysis of complex GBs and other interfaces, aberration-corrected scanning transmission electron microscopy (STEM) has been a powerful tool that provides atomic-resolution high-angle annular-dark-field (HAADF) imaging,^[3,16,20–24] while electron energy-loss spectroscopy (EELS) core-loss and fine-structure analyses provide atomic-resolution chemical maps and bonding information.^[25] While conventional STEM–EELS is limited to an energy resolution of around 300 meV, modern electron monochromators are capable of 3 meV resolution.^[26] More critically, atomic-scale spatial resolution can be achieved alongside this energy resolution, enabling direct probing of vibrational properties,^[22,27–30] paving the way to correlate the vibrational properties of the GB directly to the chemical and structural properties.

E. R. Hoglund, S. Makarem, J. M. Howe
Department of Materials Science and Engineering
University of Virginia
Charlottesville, VA 22904, USA
E-mail: erh3cq@virginia.edu

D.-L. Bao, A. O'Hara, S. T. Pantelides
Department of Physics and Astronomy
Vanderbilt University
Nashville, TN 37235, USA
E-mail: pantelides@vanderbilt.edu

T. W. Pfeifer, M. S. B. Hoque, P. E. Hopkins
Department of Mechanical and Aerospace Engineering
University of Virginia
Charlottesville, VA 22904, USA
E-mail: peh4v@virginia.edu

J. A. Hachtel
Center for Nanophase Materials Sciences
Oak Ridge National Laboratory
Oak Ridge, TN 37830, USA
E-mail: hachtelja@ornl.gov

 The ORCID identification number(s) for the author(s) of this article can be found under <https://doi.org/10.1002/adma.202208920>.

© 2023 The Authors. Advanced Materials published by Wiley-VCH GmbH. This is an open access article under the terms of the Creative Commons Attribution License, which permits use, distribution and reproduction in any medium, provided the original work is properly cited.

DOI: 10.1002/adma.202208920

Here, we examine a prototypical, highly complex, 10° [001] symmetric-tilt GB in SrTiO_3 using aberration-corrected and monochromated STEM imaging and EELS combined with DFT calculations, which are just manageable by computing power, for mutual validation. STEM imaging and core-loss EELS are used to directly measure the changes in stoichiometry and crystal structure that occur in and around the GB dislocation cores. The atomistic model of the GB is too large for conventional DFT relaxation, so the STEM/EELS data are used to facilitate the construction of the supercell, including local nonstoichiometry, that enables DFT calculations. Furthermore, energy-loss near-edge fine-structure (ELNES) analyses of the Ti and O edges at the GB together with DFT calculations reveal how the structural and chemical changes influence the bonding. Finally, monochromated EELS is used to probe the vibrations directly in the dislocation cores (intracore vibrations) as well as between the dislocation cores (intercore vibrations). Localized vibrational signatures are observed, which, through DFT calculations, are attributed to modes localized to GB dislocation-core atoms with unique environments.

2. Results

We begin by measuring the atomic structure and stoichiometry of the 10° GB using aberration-corrected STEM imaging and core-loss EELS spectroscopy. An HAADF image of this GB is shown in **Figure 1a** and **Figure S1** (Supporting Information)^[31,32] and a zoom in of the dotted white box is shown in **Figure 1b**. The corresponding EELS-derived chemical maps are shown in **Figure 1d–g**. Analysis of these data helped construct an atomistic model of the GB core (see details in **Figure S8** in the Supporting Information), optimized by DFT calculations, shown in **Figure 1c**.

The image in **Figure 1a** shows regularly spaced dislocations along the GB with markedly lower intensity than the grains, indicating a lower mass density. **Figure 1a,b** demonstrates that the GB has different coordinations than the grains. For instance, there are cations in the dislocation cores with projected threefold coordination, whereas bulk SrTiO_3 cations have a projected fourfold coordination.

The EELS of **Figure 1d–h** shows that the lower mass density at dislocation cores corresponds to Sr deficiency and Ti

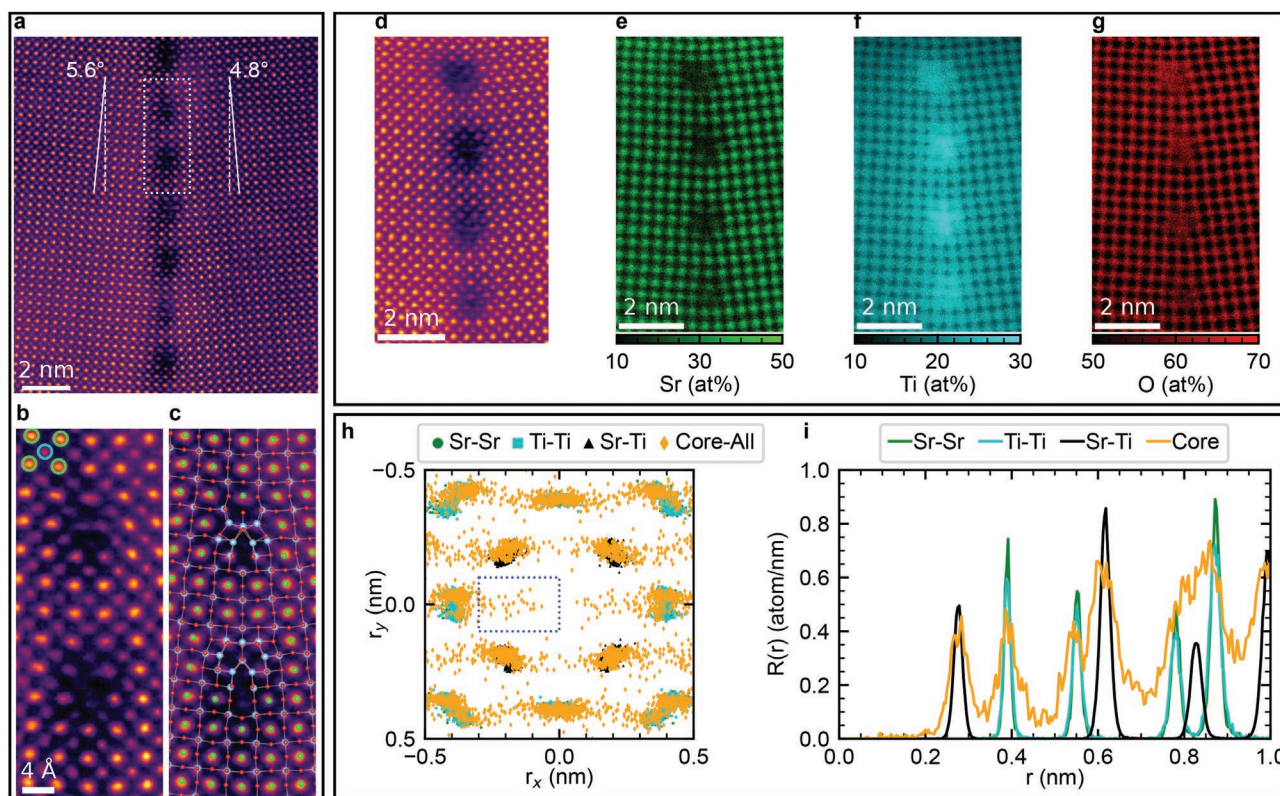


Figure 1. Local atomic positions and stoichiometry at a 10° GB. a) HAADF image showing regularly spaced dislocation cores at a GB. b) An enlarged region of the white box in (a). c) Model of GB atomic positions based on the HAADF and EELS data. Annotated atom colors in (b) are green for Sr, cyan for Ti, and red for O. d) Reference HAADF and e–g) semiquantitative compositions of Sr (e), Ti (f), and O (g). h) The 2D nearest-neighbor distribution for (green) Sr–Sr, (cyan) Ti–Ti, and (black) Sr–Ti, shows well-defined structure in the grains. Also shown is the (orange) nearest-neighbor distribution for atomic columns in the intracore regions created from all atomic columns in the image, which shows the nearest neighbors with smaller bond distances than the grain. The blue dotted box indicates atoms with shorter projected distance than in the grains, which indicates local changes in bond distance and/or coordination. i) The radial distribution function formed from the nearest-neighbor distances in (h) further shows that the grains have well-defined nearest-neighbor peaks, while at the dislocations the probability is diffuse with nonzero minima and distances less than 0.2 nm .

enrichment, while the oxygen content at the cores is as in the grains, as also seen in Figure 1c and consistent with findings for other SrTiO₃ GBs.^[31,32] We also note that the dislocation-core Ti and O signals are diffuse, compared with clear atomic columns in the grains, which suggests position variation of atoms in the projected direction.

To correlate the change in stoichiometry to the local coordination at the cores, we identify the positions of cation columns in the HAADF image, shown in Figure 1a, and separate them into Sr and Ti sublattices in the grains, and atomic columns in the dislocation cores (positions of atoms shown in Figure S2 in the Supporting Information). With the defined sublattices, we can better understand local structure through the 2D projected nearest-neighbor distribution and radial distribution function (RDF), shown in Figure 1h,i. The grains show well-defined crystalline behavior within and between the Sr and Ti sublattices. By contrast, the nearest-neighbor distribution of atoms in the GB dislocation cores show streaking along the direction normal to the boundary plane (*x*), without comparable streaking in the parallel plane (*y*), and have smaller projected nearest-neighbor distances than observed in the grains. The broader nearest-neighbor distribution is also reflected in the RDF in Figure 1i as broader nearest-neighbor peaks and a continuum back-

ground, illustrating that GB atoms have different coordinations from grain atoms.

Another critical contribution to the characteristics of a GB is bonding within the dislocations. Since the compositional analysis revealed that the dislocation cores comprise primarily Ti and O, we examine the spatial distribution of the Ti-L₂₃ and O-K core-loss ELNES to understand the local bonding (Figure 2). Here, we consider three different regions: intracore, intercore, and the bulk SrTiO₃ grains on either side. Figure 2a shows a reference HAADF image simultaneously acquired during the ELNES acquisition, which we use to mask (red) intracore, (cyan) intercore, and (black) grain regions shown in Figure 2b. The average Ti-L₂₃ and O-K edge spectra from the regions shown in Figure 2b are shown in Figure 2c,d, respectively. The Ti-L₂₃ spectra (Figure 2c) from the grains show well-defined *t*_{2g} and *e*_g peaks that result from the octahedral crystal-field splitting of Ti d-orbitals. The splitting of the *t*_{2g} and *e*_g peaks decreases to nearly one peak in the intracore spectrum for both the Ti-L₃ and Ti-L₂ edges. The intercore Ti-L₂₃ fine structure is an intermediate of the grains and intracore, having smaller *t*_{2g}-*e*_g splitting than the grains but more *t*_{2g}-*e*_g splitting than the dislocation cores, which shows that strain partially redistributes electronic states. The low intensity of the second peak in

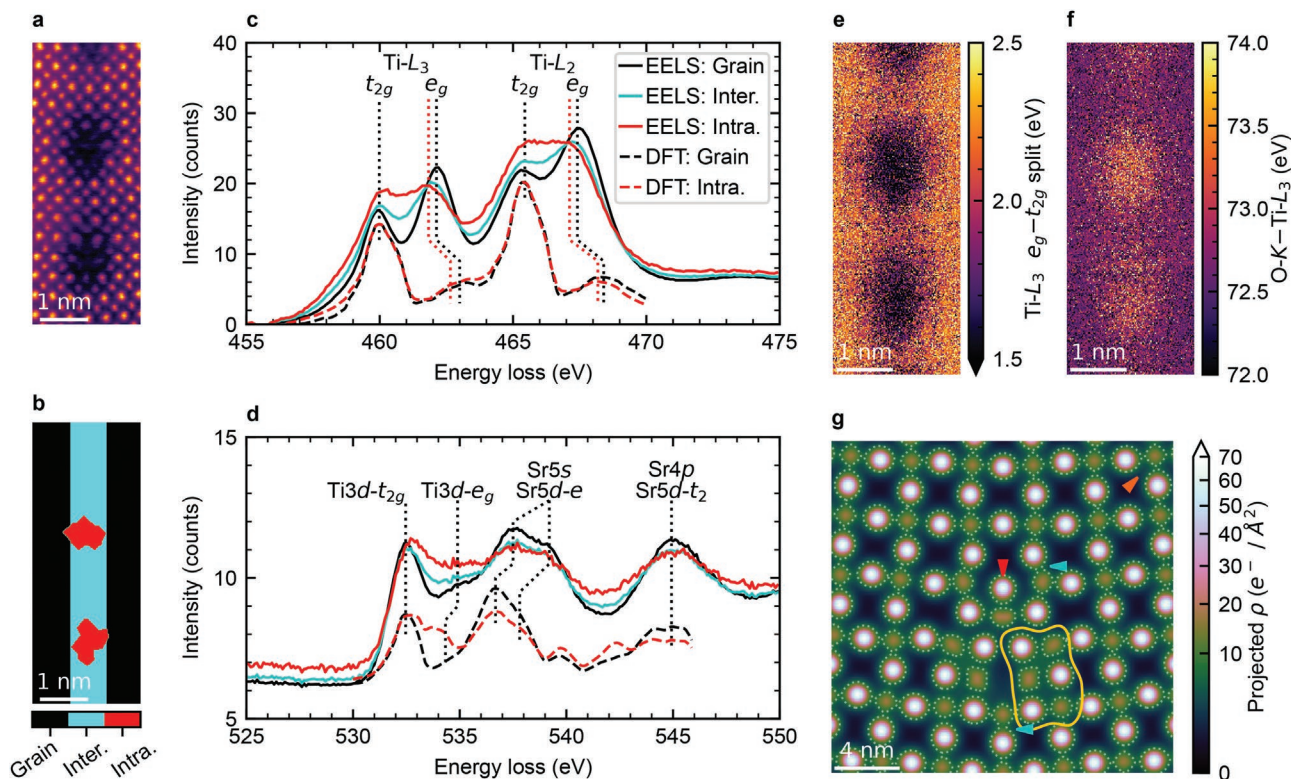


Figure 2. Local bonding at a 10° GB. a) HAADF reference signal acquired during the STEM spectrum image of the 10° GB. b) Masks highlighting atom columns located in the (red) intracore, (cyan) intercore, and (black) grain are used to create the average Ti-L₂₃ edge (c) and O-K edge (d) core-loss spectra from the respective regions (the dashed curves are DFT-calculated spectra). The labels in (d) indicate the neighboring-cation orbital content of the final states; all of them also contain O 2p. Z+1 DFT calculations from the grain and intracore region are shown in (c,d) as dashed lines and show similar Ti-L₂₃ *t*_{2g}-*e*_g splitting and O-K ELNES intensity changes as the experimental data. e) Maps of the Ti-L₂₃ *t*_{2g}-*e*_g splitting show the convergence from well-defined *t*_{2g} and *e*_g peaks into weakly split peaks. f) The difference between the O-K and Ti-L₃ onset energies shows higher values at the dislocation cores. g) Projected valence-charge density calculated using DFT. Regions of unique charge density are highlighted indicating (cyan arrow) increased orbital overlap, (red arrow) anisotropically bonded, and (gold outline) rock salt packing are annotated and show orbital redistributions different than found in the (orange arrow) grains.

and the large t_{2g} - e_g splitting in the DFT grain and dislocation-core Ti-L_{2,3} spectra are caused by the fact that both spectra were calculated in the very large supercell shown in Figure S8 (Supporting Information), which requires a practical choice for the level of accuracy. A higher-accuracy calculation of the Ti-L₂ Z+1 spectrum using a single-crystal SrTiO₃ supercell (Figure S12, Supporting Information) features a significant increase in the e_g peak's intensity and a reduction of the t_{2g} - e_g splitting, both of which are better matches to the measured EELS shown in Figure 2. A similar correction would be expected in a higher-accuracy spectrum in the dislocation core. A map of the Ti-L_{2,3} t_{2g} - e_g splitting in the GB, shown in Figure 2e, reveals a gradual change from the grain to the GB, with the GB dislocation cores having the largest change in electronic structure.

In the O-K edge, shown in Figure 2d, the peaks related to Ti 3d-O 2p orbital transitions in the grains, intercore, and intracore regions change intensity and approach a more continuous spectrum. The changes in splitting and redistribution are a direct result of the different coordinations and varying geometric distortions observed in Figure 1. The onset energies of the EELS are also different in each region, suggesting different core-electron binding energies. The relative onset energies between the Ti-L_{2,3} and O-K are mapped in Figure 2f. Prior measurements of SrTiO₃ GBs showing similar stoichiometry and ELNES changes suggest a reduction from Ti⁴⁺ to Ti³⁺ at the dislocation cores.^[33–35] The intensity redistribution in both the Ti-L_{2,3} and O-K edges represent a redistribution in orbital energies, which is tied closely to the structural and stoichiometric changes shown in Figure 1.

To achieve deeper insights for the observed redistributions in electronic states, we performed DFT calculations on a DFT-relaxed atomistic GB model, a cropped region of which is shown in Figure 1c (see also Figure S8 in the Supporting Information). First, we used the Z+1 approximation to calculate the ELNES features in the grains and at the intracore regions, shown in Figure 2c,d.^[36] The calculated Ti-L_{2,3} ELNES duplicates the decrease in the measured t_{2g} - e_g splitting and the

redistributions of states between and around the O-K t_{2g} and e_g peaks. Likewise, agreement of intensity redistribution in the O-K edge is found, demonstrating that the atomistic model and theoretical results are representative of the real GB dislocations.

We further examined the calculated GB valence-charge-density map, shown in Figure 2g, to understand the redistribution of bonding orbitals at the GB. To focus on the TiO plane bonding, the map is calculated using the DFT real-space valence-charge density integrated from the TiO₂ plane to halfway between the SrO and TiO₂ planes (i.e., 1/2 to 1/4 of the unit cell, Figures S10 and S11, Supporting Information) along the z-direction. The typical bulk SrTiO₃ perovskite is highlighted in the top right corner with an orange arrow. The grains show well-separated isosurface bounding atoms, which is typical of ionic materials. Three patterns of orbital redistribution relative to the grain are seen at the GB: regions of rock-salt-packed TiO with charge density between ions (annotated in (g) with a gold outline), regions of increased orbital overlap revealed by higher charge density between ion cores (cyan arrows), and regions where charge appears more localized on ions and anisotropically redistributed (red arrows). The broadening and decreased splitting of ELNES features at the GB relative to the grains reflects a complex redistribution of orbitals occurring at the GB in multiple ways. Therefore, the GB does not only exhibit different symmetries and concentrations, but the bonding between Ti and O atoms is stronger in some regions, weaker in others, and altogether irregular.

Having shown that the structure, stoichiometry, and bonding at the GB and dislocation cores are different from those in the grains, we now correlate these differences to localized changes in the atomic vibrations at the GB. To access highly localized vibrations at the 10° GB, we use monochromated STEM-EELS in the off-axis geometry, as shown in Figure S6b (Supporting Information). The off-axis geometry results in an asymmetric annular dark-field (aADF) signal. The aADF image of the 10° GB, shown in Figure 3a, exhibits contrast reversal relative to the HAADF images in Figures 1 and 2. The higher aADF

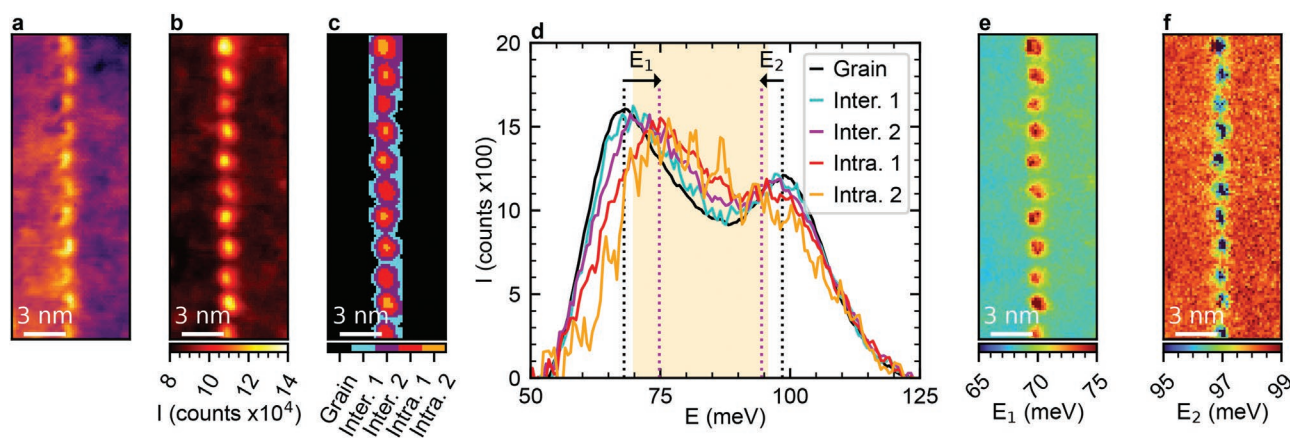


Figure 3. Localized vibrational response of a 10° GB. a) aADF image and b) total inelastic intensity from off-axis signal. c) Sequence of masks generated from total inelastic intensity to selectively probe different degrees of intracore vibrational spectra. d) Representative spectra of the masks in (c), showing a significant and continuous shift of the two peaks (labeled E₁ and E₂) as the region transitions from grain (black) to intercore (blue/purple) to intracore (red/orange). The gold spans in (d) mark the Reststrahlen band in the bulk material, emphasizing a region where vibrational states redistribute to in the intracore signal. e,f) Fit results for the peak energy of E₁ (e) and E₂ (f) showing localized blueshifts of E₁ and similarly localized redshifts of E₂.

intensity at the intracore regions is likely from static disorder. It is also observed in the total off-axis EELS signal shown in Figure 3b, which further emphasizes the environmental disorder of atoms at the GB relative to the grains.^[37]

To probe the grain, intercore, and intracore regions, we use the total EELS intensity to mask five distances from the dislocation core, as shown in Figure 3c. The average vibrational response from each characteristic region is shown in Figure 3d. Significant differences between the grain, intercore, and intracore vibrational responses are readily observed. In the grain (black), there are two primary peaks at ≈ 68 meV (labeled E_1) and ≈ 99 meV (labeled E_2), which are consistent with known phonon modes from bulk SrTiO₃ originating from displacements of the Ti and O sublattices (E_1 : second longitudinal optic (LO2)/third transverse optic phonons, E_2 : LO3 phonon).^[38] However, as we transition from the grain (black) to the intercore region (blue/purple), the E_1 peak blueshifts, while the E_2 peak redshifts. The maximum shifts occur at the intracore region (red/orange), with fitted energies ≈ 75 and ≈ 94 meV, respectively. The peak fitting is applied to the entire spectrum image, which is shown for E_1 in Figure 3e and E_2 in Figure 3f (fitting details shown in Figure S7 in the Supporting Information). The high spatial-spectral resolution analysis of monochromated STEM-EELS enables us to see that the vibrational shifts match the spatial distribution of the aADF intensity in Figure 3a as well as

the different chemistries and fine-structure maps in Figures 1 and 2, respectively. The agreement shows a clear distinction between the grain, intercore, and intracore regions.

The peak shifts in the vibrational response can be attributed to the Ti enrichment, coordination change, and bonding changes at the GB, as observed in Figures 1 and 2. Similar localized effects are observed at antiphase boundaries where Ti–Ti neighbors lead to softening of the antiferroelectric optic modes, similar to observations at GBs in other materials.^[38,39] These results demonstrate that a redistribution of vibrational states at a GB can be directly observed with monochromated EELS with the resolution necessary to correlate local structure, chemistry, and vibration characteristics of different regions at a GB.

To gain further insight into the vibrational shifts observed in Figure 3, we perform a nonnegative matrix factorization (NMF) decomposition of the dataset. NMF is a well-established technique that can provide highly informative visualizations of hyperspectral EELS acquisitions, by reducing the dataset into a linear combination of spatial abundance maps of spectral features.^[25] Figure 4a–c shows a two-component NMF decomposition of the off-axis 10° GB EELS shown and analyzed in Figure 3, with the maps shown in (a) and (b), and the spectra shown in (c). We note that the grain component spectrum in Figure 4c is nearly identical to the grain vibrational response in Figure 3d, and the core component spectrum in Figure 4c

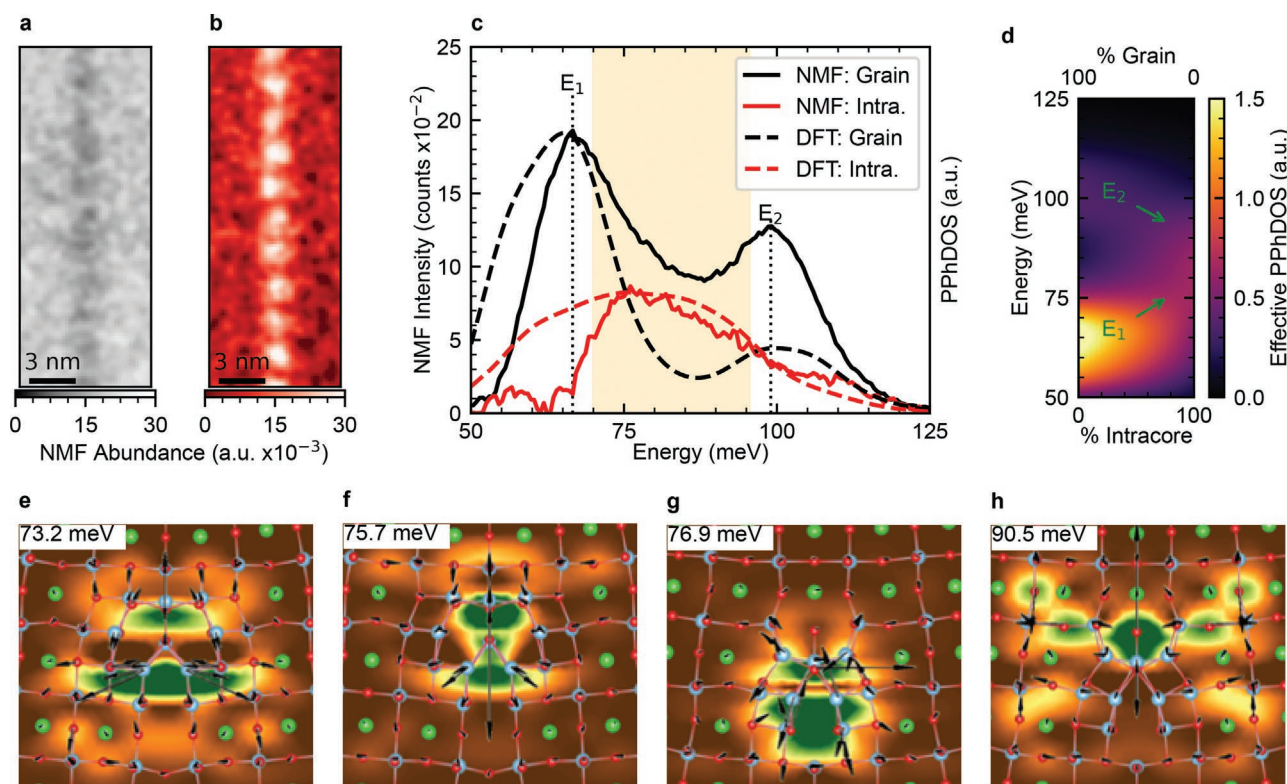


Figure 4. Local GB vibrational modes in a 10° GB. a–c) Two component NMF analysis of off-axis GB spectrum image. a,b) NMF maps show the decomposition of the spectrum-image data into a linear combination of the grain signal (a) and the core signal (b). c) The corresponding NMF spectra (solid curves) and DFT-calculated projected phonon density of states (PPhDOSs) (dashed curves) exhibit overall good agreement. The grain spectra (black) match the raw EELS grain spectrum in Figure 3, while the core spectra (red) feature an asymmetric peak with a maximum at ≈ 75 meV and a high energy tail. d) Different linear combinations of the DFT GB-dislocation core and grain PPhDOSs demonstrate that the measured vibrational spectra shown in Figure 3 can indeed be viewed as a combination of the intracore and bulk signals and varying concentrations (see also Figure S9 in the Supporting Information). e–h) Atomic displacements of vibrational modes localized within the GB cores at 73.2 (e), 75.7 (f), 76.9 (g), and 90.5 meV (h).

shows a peak at 75 meV, which is the energy that the E_1 peak shifts to in the intracore regions in Figure 3d. Furthermore, the intensity of the grain component map shown in Figure 4a is not significantly reduced at the dislocation cores, as in the average NMF abundance in the cores is only $\approx 25\%$ than the average NMF abundance in the grains (Figure S5, Supporting Information). Conversely, the intensity of the core component map in Figure 4b is almost nonexistent in the grains, with the average intensity of the core component reduced by $\approx 85\%$ compared to the intensity in the center of the intracore region. The critical implication of this finding, is that the measured signal (shown in Figure 3) is not the pure dislocation core signal, but rather a linear combination of the grain and core component spectrum at differing ratios, even with the increased localization of the off-axis EELS collection geometry. Therefore, the GB dislocations have vibrations associated with structure, nonstoichiometry, and bonding not present in the grain, but also have additional vibrations from local environments that share similarity with the perfect SrTiO_3 grain.

The nature of these localized core-component vibrational modes is unveiled using DFT calculations of projected phonon densities of states (PPhDOSs). In Figure 4c, we overlay the PPhDOS of bulk SrTiO_3 as representative of the grains and the PPhDOS in the GB core with the EELS NMF components (see discussion in Figure S9 in the Supporting Information for how PPhDOS for each region is calculated). Both PPhDOSs exhibit excellent agreement with the corresponding EELS NMF spectra, especially in the energy of the main peaks.

Moreover, the agreement helps us physically understand the peak shift occurring in Figure 3d. Figure 4d captures the behavior by showing a transition from a pure grain signal to a pure intracore signal at different weighted intensities. The superposition of grain and intracore PPhDOS accurately reproduces the E_1 peak blueshift and E_2 peak redshift (an offset spectrum visualization of the effect is shown Figure S9 in the Supporting Information).

We noted already that the GB-core NMF spectrum and the PPhDOS in Figure 4c feature a primary peak centered at ≈ 75 meV that corresponds to vibrational modes within the gold-shaded Reststrahlen band of SrTiO_3 , which ranges from 68 and 93.5 meV.^[40] As a result, the pertinent modes are localized in the GB vicinity as they cannot propagate within the grains. We can also use the DFT calculations to visualize four such modes by plotting their displacement eigenvectors in Figure 4e–g. The four modes, at eigenfrequencies 73.2 meV (e), 75.7 meV (f), 76.9 meV (g), and 90.5 meV (h), are representative of the intracore regions. The displacement amplitudes for all four modes are large at the center of the dislocation core and small at the periphery, showing a high degree of localization in the intracore region. Furthermore, the localization of each mode is related to regions of different bondings shown in Figure 2g. For example, the 73.2, 75.7, and 76.9 meV modes associated with Ti–O vibrations are localized to regions with coordination and bonding like a TiO rock salt structure. The 90.5 meV mode is localized at the anisotropically bonded oxygen. We, therefore, identify the contribution of stoichiometry, highly irregular bonding, and local symmetry to the redistribution of vibrational modes at a GB.

3. Conclusions

The influence of GB structure, stoichiometry, and bonding on atomic vibrations is often left to simulations or inferred from a collection of boundaries in bulk samples. The combination of aberration-corrected STEM, monochromated EELS, and DFT calculations reveal that a GB and GB dislocation cores have unique vibrations that are a direct result of local structure, stoichiometry, and irregular bonding. The ability to self-consistently measure and correlate coordination, chemistry, bonding, electronic states, and vibrational modes at the atomic scale enables the direct examination of single GBs that are complex in structure and composition. By unveiling the structure–chemistry–vibration relationships of GBs, their full impact on critical properties like infrared optical activity, thermal conductivity, heat capacity, and the vibrational entropy can be understood.

4. Experimental Section

Samples and Sample Preparation: The 10° and 6° SrTiO_3 bicrystals were purchased from MTI Corporation. Plane view transmission electron microscopy (TEM) samples were made using a Thermo Fisher Scientific Helios Dual Beam focused ion beam. Initial milling and cleaning were performed at 30 kV, which was sequentially decreased until a finishing energy of 2 kV.

Electron Microscopy: Aberration-corrected STEM imaging and core-loss EELS were performed on a Thermo Fisher Scientific Themis-Z STEM operating at 200 kV with a 25 mrad convergence angle. Up to third-order aberrations were corrected for imaging and spectrum imaging. Drift-corrected imaging and analysis is explained further in subsection Electron Microscopy—“Aberration- and Drift-Corrected STEM Imaging” and core-loss EELS analysis is explained further in subsection “Electron Microscopy—Atomic-Resolution Core-Loss EELS”.

Vibrational EELS were acquired at 60 keV using a Nion High-Energy Resolution Monochromated EELS STEM (HERMES) 100. Due to the low accelerating voltage used to optimize energy resolution, imaging and core-loss were conducted exclusively at the University of Virginia. A convergence semiangle of 30 mrad was used with a collection angle of 25 mrad and a dispersion 0.525 meV per channel. Spectra were acquired as 5D datasets, with one temporal (t), two spatial (x, y), one perpendicular momentum (q), and one energy-loss (E) dimensions. Alignment, denoising, and fitting procedures are explained further in subsection “Electron Microscopy—Vibrational EELS”.

Electron Microscopy—Aberration- and Drift-Corrected STEM Imaging: STEM imaging was performed using a probe current of 20 pA. Two 1024×1024 px images were acquired at 90° relative scan rotations to compensate for linear and nonlinear drift.^[41] An example of the drift correction for the image in Figure 1a is shown in Figure S1 (Supporting Information). Each image was acquired with a 64 μs dwell time. The image shown in Figure 1 was acquired with an 8 pm step size and the images in Figure S2b–d (Supporting Information) were acquired with a 16 pm step size.

Atomic columns within the grains were found and separated into Sr and Ti sublattices using Atomap.^[42] Atoms at the dislocation cores were separated into a third sublattice. The border atoms of the dislocation cores were defined by the first Sr atomic columns returning to the intensity of the grains’ Sr atomic columns. The positions for atomic columns in each sublattice were refined by first finding the center of mass within a masked region 15% to the column’s nearest neighbors. Further subpixel refinement was then iteratively performed by updating the nearest-neighbor masked region and fitting 2D Gaussians. The resulting atom positions are shown in Figure S2 (Supporting Information). The nearest-neighbor distributions were created using the cKDTree algorithm as implemented in SciPy with a radial cutoff of 3 nm.^[43] Radial

distribution functions were then calculated from the nearest-neighbor distributions by binning the nearest-neighbor distances.

Electron Microscopy—Atomic-Resolution Core-Loss EELS: Core-loss spectrum images were acquired using a probe current of 100 pA and a spectrometer collection angle of 86 mrad. A Gatan K2 detector was used to acquire core-loss spectrum images with low signal-to-noise ratio. The Ti-L₂₃, O-K, and Sr-L₂₃ edges were used for semiquantitative elemental analysis to show enrichment and depletion regions. Spectrum images were then analyzed after singular-valued-decomposition denoising and in the raw state to provide low noise data for mapping while also representing the raw data, as shown in Figures 2 and 3, respectively. Singular-valued-decomposition analysis was by nature a linear combination of singular spectra, so care needed to be taken when choosing the number of components in a system where peaks shifted gradually over many pixels. In systems in which peaks shifted dynamically, a compromise between noise and data features needed to be weighed carefully and then compared with the raw data and physics of the system. For further information on the denoising procedure, the reader is referred to Section S2.1 (Supporting Information).

Mean spectra shown in Figure 2d,e were the averages of spectra from the grains, intracore, and intercore regions acquired with a 0.1 eV per channel dispersion. Here, the intracore regions were defined by a decreased intensity of the Sr sublattice in HAADF images. The intercore regions were between the intracore regions. The intracore regions were constructed by creating Voronoi cells of the atomic columns with SciPy.^[43] Each Voronoi cell in the intracore regions was used to create a spatial mask, then the signal in each mask was averaged. The intercore region was then assigned as the remaining area ± 1 unit cell from the boundary plane.

EELS from the full spectrum images and Voronoi regions were fitted using least-square optimization, as implemented in HyperSpy.^[44] Fitting procedures for the stoichiometric mapping, ELNES mapping, and Voronoi mapping were performed in different manners and a full description of each can be found in Section S2.2 (Supporting Information).

Electron Microscopy—Vibrational EELS: The spectrum image for the GB vibrations was obtained with a sequence of 30 individual spectrum images with dwell times of 10 ms per pixel with a 2D EEL spectrum (1028 \times 130 pixels) captured for each spectrum-image pixel (total dataset size: 88 GB). The spectrum-image frame along the temporal direction was aligned using rigid registration to the total EELS signal, then averaged, providing good signal-to-noise with minimal drift distortion. The zero of the energy axis was aligned using the full-width at half-maximum of the zero-loss or quasielastic peak. Delocalized dipole scattering decayed as approximately q^{-2} with high- q signal localized to atomic length-scales.^[45] Therefore, momentum transfer >35 mrad was integrated into a single spectrum for each pixel, providing highly localized signal, as shown in Figure S6a,b (Supporting Information). The 35 mrad cutoff was chosen to maximize signal-to-noise and the localization of the signal. The energy resolution measured as the full-width at half-maximum of the on-axis zero-loss peak was 13.64 meV and the resolution of the off-axis signal measured as the full-width at half-maximum of the quasielastic peak was 16.72 meV. The quasielastic peak at 0 meV had a large nonanalytical tail that was background subtracted by fitting an exponential to two windows at 45–55 and 130–140 meV, providing spatially comparable longitudinal-optic/third-transverse-optic and third-longitudinal-optic phonon peaks.

The region-of-interest comparisons were not denoised. For peak shift mapping, the spectrum image was denoised using six components of a singular-valued decomposition before background subtraction to minimize noise and increase the integrity of background fits. In the following text, a fitting procedure was described, which is also shown in Figure S7 (Supporting Information) for a grain and intracore location. An intensity offset was measured between 275 and 280 meV, then a power-law function was fitted using two windows from 45–55 and 130–140 meV. The background was then fixed and two Gaussians to approximate the shifting of the two nonanalytical peaks were seen in Figure 3d. The first Gaussian was fitted from 62.5 to 72.5 meV with

an upper bound set on the Gaussian center at 81 meV. The second Gaussian was then fitted from 94.5 to 105 meV with the Gaussian center bounded between 90 and 99 meV.

Before NMF, a kernel filter was applied to the raw data and then background subtraction was performed. Kernel filtering enhanced the signal-to-noise, providing more reliable background subtraction and less artifact in the NMF from the fitting procedure. NMF performed after background subtraction provided better sensitivity to changes in the optical phonon peaks and suppressed sensitivity to the high-intensity low-energy features.

Calculations: The DFT calculations were performed with the Vienna Ab initio Simulation Package^[46] using the projected-augmented wave method.^[47,48] The local density approximation (LDA)^[49] was adopted for the exchange-correlation functional based on the good performance of LDA on phonon calculations at the Γ point.^[22] The plane-wave basis energy cutoff was 500 eV for structural optimization, charge density, and Z+1 calculations, but 400 eV for the phonon calculations because of the calculational cost required by the big cell. The calculational supercell contained two cubic-SrTiO₃ domains with $\approx 10^\circ$ tilt angles separated by two parallel GBs. The GB consisted of two alternating distorted cores (intracore) and deformed cubic SrTiO₃ lattices (intercore). To reduce the number of the modeling atoms, there were only two atomic layers along the z-direction, i.e., one SrTiO₃ primitive cell in thickness, with a net number of 1130 atoms in the supercell, which was at the edge of practicality. The lattice parameters of the supercell were 77.7, 42.7, and 3.87 Å along the x-, y-, and z-directions. The structure was relaxed until the interatomic forces were less than 0.02 eV Å⁻¹. The k-samplings were 1 \times 1 \times 3 for structural optimization and charge-density calculations, 1 \times 1 \times 1 for phonon calculations, and 3 \times 3 \times 12 for the Z+1 calculations in the GB supercell. The grain PhDOS was calculated using the GB supercell, by projecting the eigenvectors in the (110) plane that was perpendicular to the electron beam. The intracore PhDOS was obtained using the GB supercell, by projecting 152 intracore atoms' vibrations in the (110) plane. The core-loss EELS was simulated using the Z+1 approximation, i.e., calculating the PDOS on one intracore oxygen atom that was replaced with fluorine and on one intracore titanium atom that was replaced with vanadium. In the theoretical spectra shown in Figure 2c,d, "DFT-grain" meant 100% grain, whereas "DFT-intra" meant a sum of 30% intracore PDOS and 70% grain PDOS on the corresponding atoms. The ratio was adjusted to optimize agreement with the experimental EELS. The phonon DOS was used as a good approximation to phonon EELS as it was found to be satisfactory.^[22,28] Higher level phonon EELS simulations^[45,50] were not practical for the present large supercell. The Z+1 calculation for Ti in the single-crystal SrTiO₃ supercell was based on a 3 \times 3 \times 3 supercell of *Pm3m* SrTiO₃ (135 atoms). The k-samplings were 3 \times 3 \times 3 for the charge density and 4 \times 4 \times 4 for the density-of-states' calculations. The Z+1 method had proved to be quite accurate compared to methods that included a real core hole or to experimental data.^[51,52] Higher levels of approximations were not practical for the present large supercell.

Supporting Information

Supporting Information is available from the Wiley Online Library or from the author.

Acknowledgements

E.R.H. and D.-L.B. contributed equally to this work. Monochromated EELS research was supported by the Center for Nanophase Materials Sciences (CNMS), which is a DOE Office of Science User Facility using instrumentation within ORNL's Materials Characterization Core provided by UT-Battelle, LLC, under Contract No. DE-AC05-00OR22725 with the DOE and sponsored by the Laboratory Directed Research and Development Program of Oak Ridge National Laboratory, managed

by UT-Battelle, LLC, for the U.S. Department of Energy. Aberration-corrected drift-corrected STEM imaging and core-loss EELS were supported by the Army Research Office, Grant No. W911NF-21-1-0119. Utilization of the Thermo Fisher Scientific Themis-Z STEM and Helios dual-beam focus ion beam instruments within UVA's Nanoscale Materials Characterization Facility (NMCF) was fundamental to this work. The authors thank Helge Heinrich for aiding in TEM sample preparation. Theory at Vanderbilt University (D.-L.B., A.O., and S.T.P.) was supported by the U.S. Department of Energy, Office of Science, Basic Energy Sciences, Materials Science and Engineering Directorate Grant No. DE-FG02-09ER46554 and by the McMinn Endowment at Vanderbilt University. D.-L.B. was partially supported by the K. C. Wong Education Foundation of the Chinese Academy of Sciences. Calculations were performed at the National Energy Research Scientific Computing Center (NERSC), a U.S. Department of Energy Office of Science User Facility located at Lawrence Berkeley National Laboratory, operated under Contract No. DE-AC02-05CH11231.

Conflict of Interest

The authors declare no conflict of interest.

Author Contributions

E.R.H. and J.A.H. designed the experiments and performed all acquisition and analysis of STEM data. D.-L.B., A.O., and S.T.P. contributed all density-functional-theory calculations. E.R.H., D.-L.B., A.O., T.W.P., M.S.B.H., S.M., J.M.H., S.T.P., P.E.H., and J.A.H. had expertise and understanding of GB and vibrational physics. E.R.H. wrote the paper and the Supporting Information. All authors contributed to the direction and revision of the paper. Regarding reprints and permissions, please contact E.R.H., S.T.P., P.E.H., or J.A.H. Please contact any corresponding author for financial or nonfinancial questions.

Data Availability Statement

The data that support the findings of this study are available from the corresponding author upon reasonable request.

Keywords

dislocations, grain boundaries, local atomic vibrations, phonons, vibrational states

Received: September 27, 2022

Revised: November 25, 2022

Published online: February 10, 2023

- [1] P. Lejček, S. Hofmann, M. Všianská, M. Šob, *Acta Mater.* **2021**, *206*, 116597.
- [2] A. M. van der Zande, P. Y. Huang, D. A. Chenet, T. C. Berkelbach, Y. You, G.-H. Lee, T. F. Heinz, D. R. Reichman, D. A. Muller, J. C. Hone, *Nat. Mater.* **2013**, *12*, 554.
- [3] M. Kim, G. Duscher, N. D. Browning, K. Sohlberg, S. T. Pantelides, S. J. Pennycook, *Phys. Rev. Lett.* **2001**, *86*, 4056.
- [4] A. Sood, R. Cheaito, T. Bai, H. Kwon, Y. Wang, C. Li, L. Yates, T. Bougher, S. Graham, M. Asheghi, M. Goorsky, K. E. Goodson, *Nano Lett.* **2018**, *18*, 3466.
- [5] S. Fujii, T. Yokoi, C. A. J. Fisher, H. Moriwake, M. Yoshiya, *Nat. Commun.* **2020**, *11*, 1854.

- [6] H. Dong, B. Wen, R. Melnik, *Sci. Rep.* **2015**, *4*, 7037.
- [7] B. M. Foley, H. J. Brown-Shaklee, J. C. Duda, R. Cheaito, B. J. Gibbons, D. Medlin, J. F. Ihlefeld, P. E. Hopkins, *Appl. Phys. Lett.* **2012**, *101*, 231908.
- [8] M. Lewin, C. Baeumer, F. Gunkel, A. Schwedt, F. Gaussmann, J. Wueppen, P. Meuffels, B. Jungbluth, J. Mayer, R. Dittmann, R. Waser, T. Taubner, *Adv. Funct. Mater.* **2018**, *28*, 1802834.
- [9] P. R. Cantwell, M. Tang, S. J. Dillon, J. Luo, G. S. Rohrer, M. P. Harmer, *Acta Mater.* **2014**, *62*, 1.
- [10] S. I. Kim, K. H. Lee, H. A. Mun, H. S. Kim, S. W. Hwang, J. W. Roh, D. J. Yang, W. H. Shin, X. S. Li, Y. H. Lee, G. J. Snyder, S. W. Kim, *Science* **2015**, *348*, 109.
- [11] R. Ramesh, D. G. Schlom, *Nat. Rev. Mater.* **2019**, *4*, 257.
- [12] S. Das, Y. L. Tang, Z. Hong, M. A. P. Gonçalves, M. R. McCarter, C. Klewe, K. X. Nguyen, F. Gómez-Ortiz, P. Shafer, E. Arenholz, V. A. Stoica, S.-L. Hsu, B. Wang, C. Ophus, J. F. Liu, C. T. Nelson, S. Saremi, B. Prasad, A. B. Mei, D. G. Schlom, J. Íñiguez, P. García-Fernández, D. A. Muller, L. Q. Chen, J. Junquera, L. W. Martin, R. Ramesh, *Nature* **2019**, *568*, 368.
- [13] G. Lu, S. Li, X. Ding, J. Sun, E. K. H. Salje, *npj Comput. Mater.* **2020**, *6*, 145.
- [14] R. H. Ewing, *Acta Metall.* **1971**, *19*, 1359.
- [15] Q. Zhu, A. Samanta, B. Li, R. E. Rudd, T. Frolov, *Nat. Commun.* **2018**, *9*, 467.
- [16] T. Meiners, T. Frolov, R. E. Rudd, G. Dehm, C. H. Liebscher, *Nature* **2020**, *579*, 375.
- [17] R. Hanus, A. Garg, G. J. Snyder, *Commun. Phys.* **2018**, *1*, 78.
- [18] M. Hashimoto, H. Ichinose, Y. Ishida, R. Yamamoto, M. Doyama, *Jpn. J. Appl. Phys.* **1980**, *19*, 1045.
- [19] M. Hashimoto, Y. Ishida, R. Yamamoto, M. Doyama, *Acta Metall.* **1981**, *29*, 617.
- [20] Z. Wang, M. Saito, K. P. McKenna, L. Gu, S. Tsukimoto, A. L. Shluger, Y. Ikuhara, *Nature* **2011**, *479*, 380.
- [21] J. Wei, B. Feng, R. Ishikawa, T. Yokoi, K. Matsunaga, N. Shibata, Y. Ikuhara, *Nat. Mater.* **2021**, *20*, 951.
- [22] E. R. Hoglund, D.-L. Bao, A. O'Hara, S. Makarem, Z. T. Piontkowski, J. R. Matson, A. K. Yadav, R. C. Haislmaier, R. Engel-Herbert, J. F. Ihlefeld, J. Ravichandran, R. Ramesh, J. D. Caldwell, T. E. Beechem, J. A. Tomko, J. A. Hachtel, S. T. Pantelides, P. E. Hopkins, J. M. Howe, *Nature* **2022**, *601*, 556.
- [23] C. Domínguez, A. B. Georgescu, B. Mundet, Y. Zhang, J. Fowle, A. Mercy, A. Waelchli, S. Catalano, D. T. L. Alexander, P. Ghosez, A. Georges, A. J. Millis, M. Gibert, J.-M. Triscone, *Nat. Mater.* **2020**, *19*, 1182.
- [24] C. M. Barr, E. Y. Chen, J. E. Nathaniel, P. Lu, D. P. Adams, R. Dingreville, B. L. Boyce, K. Hattar, D. L. Medlin, *Sci. Adv.* **2022**, *8*, 13.
- [25] R. F. Egerton, *Electron Energy-Loss Spectroscopy in the Electron Microscope*, Springer, Boston, MA, USA **2011**.
- [26] N. Dellby, T. Lovejoy, G. Corbin, N. Johnson, R. Hayner, M. Hoffman, P. Hrncrik, B. Plotkin-Swing, D. Taylor, O. Krivanek, *Microsc. Microanal.* **2020**, *26*, 1804.
- [27] K. Venkatraman, B. D. A. Levin, K. March, P. Rez, P. A. Crozier, *Nat. Phys.* **2019**, *15*, 1237.
- [28] F. S. Hage, G. Radtke, D. M. Kepaptsoglou, M. Lazzeri, Q. M. Ramasse, *Science* **2020**, *367*, 1124.
- [29] Z. Cheng, R. Li, X. Yan, G. Jernigan, J. Shi, M. E. Liao, N. J. Hines, C. A. Gadre, J. C. Idrobo, E. Lee, K. D. Hobart, M. S. Goorsky, X. Pan, T. Luo, S. Graham, *Nat. Commun.* **2021**, *12*, 6901.
- [30] R. Senga, Y.-C. Lin, S. Morishita, R. Kato, T. Yamada, M. Hasegawa, K. Suenaga, *Nature* **2022**, *603*, 68.
- [31] H. Du, C.-L. Jia, L. Houben, V. Metlenko, R. A. De Souza, R. Waser, J. Mayer, *Acta Mater.* **2015**, *89*, 344.
- [32] P. Gao, R. Ishikawa, B. Feng, A. Kumamoto, N. Shibata, Y. Ikuhara, *Ultramicroscopy* **2018**, *184*, 217.

- [33] E. Stoyanov, F. Langenhorst, G. Steinle-Neumann, *Am. Mineral.* **2007**, *92*, 577.
- [34] M. Varela, M. P. Oxley, W. Luo, J. Tao, M. Watanabe, A. R. Lupini, S. T. Pantelides, S. J. Pennycook, *Phys. Rev. B* **2009**, *79*, 085117.
- [35] I. Tanaka, T. Mizoguchi, T. Yamamoto, *Jpn. J. Appl. Phys.* **2005**, *88*, 2013.
- [36] R. Buczko, G. Duscher, S. J. Pennycook, S. T. Pantelides, *Phys. Rev. Lett.* **2000**, *85*, 2168.
- [37] J. M. Howe, B. Fultz, S. Miao, in *Characterization of Materials* (Ed: E. N. Kaufmann), John Wiley & Sons, Inc., Hoboken, NJ, USA **2012**.
- [38] B. Han, R. Shi, H. Peng, Y. Lv, R. Qi, Y. Li, J. Zhang, J. Du, P. Yu, P. Gao, *ArXiv: 2203.01772*, **2022**.
- [39] M. Wu, X. Zhang, X. Li, K. Qu, Y. Sun, B. Han, R. Zhu, X. Gao, J. Zhang, K. Liu, X. Bai, X.-Z. Li, P. Gao, *Nat. Commun.* **2022**, *13*, 216.
- [40] Y. Xie, H.-Y. Cao, Y. Zhou, S. Chen, H. Xiang, X.-G. Gong, *Sci. Rep.* **2015**, *5*, 10011.
- [41] C. Ophus, J. Ciston, C. T. Nelson, *Ultramicroscopy* **2016**, *162*, 1.
- [42] M. Nord, P. E. Vullum, I. MacLaren, T. Tybell, R. Holmestad, *Adv. Struct. Chem. Imaging* **2017**, *3*, 9.
- [43] P. Virtanen, R. Gommers, T. E. Oliphant, M. Haberland, T. Reddy, D. Cournapeau, E. Burovski, P. Peterson, W. Weckesser, J. Bright, S. J. van der Walt, M. Brett, J. Wilson, K. J. Millman, N. Mayorov, A. R. J. Nelson, E. Jones, R. Kern, E. Larson, C. J. Carey, Í. Polat, Y. Feng, E. W. Moore, J. VanderPlas, D. Laxalde, J. Perktold, R. Cimrman, I. Henriksen, E. A. Quintero, C. R. Harris, et al., *Nat. Methods* **2020**, *17*, 261.
- [44] F. de la Peña, V. T. Fauske, P. Burdet, E. Prestat, P. Jokubauskas, M. Nord, T. Ostasevicius, K. E. MacArthur, M. Sarahan, D. N. Johnstone, J. Taillon, A. Eljarrat, V. Migunov, J. Caron, T. Furnival, S. Mazucco, T. Aarholt, M. Walls, T. Slater, F. Winkler, B. Martineau, G. Donval, R. McLeod, E. R. Hoglund, I. Alxneit, I. Hjorth, T. Henninen, L. F. Zagonel, A. Garmannslund, A. Skorikov, **2018**, hyperspy v1.4.1, <https://doi.org/10.5281/zenodo.1469364>.
- [45] R. Senga, K. Suenaga, P. Barone, S. Morishita, F. Mauri, T. Pichler, *Nature* **2019**, *573*, 247.
- [46] G. Kresse, J. Furthmüller, *Phys. Rev. B* **1996**, *54*, 11169.
- [47] P. E. Blöchl, *Phys. Rev. B* **1994**, *50*, 17953.
- [48] G. Kresse, D. Joubert, *Phys. Rev. B* **1999**, *59*, 1758.
- [49] J. P. Perdew, A. Zunger, *Phys. Rev. B* **1981**, *23*, 5048.
- [50] P. M. Zeiger, J. Ruzs, *Phys. Rev. Lett.* **2020**, *124*, 025501.
- [51] R. Buczko, G. Duscher, S. J. Pennycook, S. T. Pantelides, *Phys. Rev. Lett.* **2000**, *85*, 2168.
- [52] W. Luo, M. Varela, J. Tao, S. J. Pennycook, S. T. Pantelides, *Phys. Rev. B* **2009**, *79*, 052405.